Monthly Notices of the ROYAL ASTRONOMICAL SOCIETY

MNRAS **500,** 54–65 (2021)
Advance Access publication 2020 October 16

doi:10.1093/mnras/staa3228

Asteroseismic modelling of solar-type stars: a deeper look at the treatment of initial helium abundance

Benard Nsamba,[1,2]★ Nuno Moedas,[2,3] Tiago L. Campante,[2,3] Margarida S. Cunha,[2,4] Antonio García Hernández,[5,6] Juan C. Suárez,[5,6] Mário J. P. F. G. Monteiro,[2,3] João Fernandes,[7] Chen Jiang[8] and Babatunde Akinsanmi[2,3]

[1] *Max-Planck-Institut für Astrophysik, Karl-Schwarzschild-Str. 1, D-85748 Garching, Germany*
[2] *Instituto de Astrofísica e Ciências do Espaço, Universidade do Porto, Rua das Estrelas, PT4150-762 Porto, Portugal*
[3] *Departamento de Física e Astronomia, Faculdade de Ciências da Universidade do Porto, Rua do Campo Alegre, s/n, PT4169-007 Porto, Portugal*
[4] *School of Physics and Astronomy, University of Birmingham, Birmingham B15 2TT, UK*
[5] *Department of Theoretical Physics and Cosmology, University of Granada (UGR), E-18071 Granada, Spain*
[6] *Instituto de Astrofísica de Andalucía (CSIC), Glorieta de la Astronomía S/N, E-18008 Granada, Spain*
[7] *CITEUC, Department of Mathematics, Geophysical and Astronomical Observatory, Univ Coimbra, Apartado 3008, EC Santa Cruz, 3001 - 501 Coimbra, Portugal*
[8] *School of Physics and Astronomy, Sun Yat-sen University, 2 Daxue Road, Tangjia, Zhuhai 519082, Guangdong Province, China*

Accepted 2020 October 12. Received 2020 October 8; in original form 2020 August 10

ABSTRACT

Detailed understanding of stellar physics is essential towards a robust determination of stellar properties (e.g. radius, mass, and age). Among the vital input physics used in the modelling of solar-type stars which remain poorly constrained, is the initial helium abundance. To this end, when constructing stellar model grids, the initial helium abundance is estimated either (i) by using the semi-empirical helium-to-heavy element enrichment ratio, ($\Delta Y/\Delta Z$), anchored to the standard big bang nucleosynthesis value, or (ii) by setting the initial helium abundance as a free variable. Adopting 35 low-mass, solar-type stars with multiyear *Kepler* photometry from the asteroseismic 'LEGACY' sample, we explore the systematic uncertainties on the inferred stellar parameters (i.e. radius, mass, and age) arising from the treatment of the initial helium abundance in stellar model grids. The stellar masses and radii derived from grids with free initial helium abundance are lower compared to those from grids based on a fixed $\Delta Y/\Delta Z$ ratio. We find the systematic uncertainties on mean density, radius, mass, and age arising from grids which employ a fixed value of $\Delta Y/\Delta Z$ and those with free initial helium abundance to be $\sim$ 0.9 per cent, $\sim$ 2 per cent, $\sim$ 5 per cent, and $\sim$ 29 per cent, respectively. We report that the systematic uncertainties on the inferred masses and radii arising from the treatment of initial helium abundance in stellar grids lie within the expected accuracy limits of ESA's PLATO, although this is not the case for the age.

Key words: asteroseismology – stars: evolution – stars: fundamental parameters – stars: oscillations – stars: statistics.

1 INTRODUCTION

One of the vital model inputs employed in stellar evolution codes (such as, MESA;[1] Paxton et al. 2013, 2015, 2018, GARSTEC;[2] Weiss & Schlattl 2008, YREC;[3] Demarque et al. 2008) aiding our understanding of the formation, structure, and evolution of stars are their chemical compositions. When modelling an ensemble of solar-type stars, solar metallicity mixtures are commonly adopted. This is because a good agreement exists between element abundances of the Sun and solar-type stars. However, at low metallicities, the solar-type stars get more enhanced in some elements (alpha elements) when compared to the Sun (see Adibekyan et al. 2012 for details). Based on the approach used in determining solar abundances (e.g. through the analysis of solar photospheric spectrum and meteorite) significant discrepancies exist among different surface elements (Anders & Grevesse 1989; Grevesse & Sauval 1998; Lodders 2003; Grevesse, Asplund & Sauval 2007; Asplund et al. 2009). Using spectroscopic methods, estimation of helium element abundance in solar-type stars still present vital challenges. This is because the envelope temperatures of these stars are not sufficient to excite helium, thus few or no helium lines are detectable in their spectra using spectroscopic observations. This is the origin of the challenges faced by stellar modellers in determining initial helium abundances to be used in stellar evolution models.

In order to circumvent the initial helium abundance problem when constructing stellar models, there are two approaches commonly adopted: (i) determining the initial helium abundance (Y_i) using the helium-to-heavy element enrichment ratio ($\Delta Y/\Delta Z$) anchored to the primordial big bang nucleosynthesis values (i.e. $Z_0 = 0$ and

★ E-mail: benard.nsamba@astro.up.pt
[1] Modules for Experiments in Stellar Astrophysics.
[2] Garching Stellar Evolution Code.
[3] Yale Rotating Stellar Evolution Code.

© 2020 The Author(s)
Published by Oxford University Press on behalf of the Royal Astronomical Society

Downloaded from https://academic.oup.com/mnras/article/500/1/54/5925370 by Inst. Astrofisica Andalucia CSIC user on 10 February 2021

$Y_0 = 0.2484$, Cyburt, Fields & Olive 2003) through the following expression;

$$\left(\frac{\Delta Y}{\Delta Z}\right) = \frac{Y_i - Y_0}{Z_i - Z_0} \ , \tag{1}$$

where Z_i is the initial metal abundance. This has been widely adopted in stellar grid construction, for example, Basu, Chaplin & Elsworth (2010), Metcalfe et al. (2010), Gai et al. (2011), Lebreton & Goupil (2014), Metcalfe et al. (2014), Silva Aguirre et al. (2015, 2017), Rodrigues et al. (2017), Frandsen et al. (2018), Nsamba et al. (2018a, b, 2019), Verma et al. (2019), Li et al. (2020), Serenelli et al. (2020), Jiang et al. (2020), among others. (ii) Setting free values of Y_i. These may be set to range between 0.22 and 0.34 (e.g. Mathur et al. 2012; Metcalfe et al. 2014; Verma et al. 2014; Silva Aguirre et al. 2015, 2017; Joyce & Chaboyer 2018a, 2018b; Bellinger et al. 2019; Angelou et al. 2020) or a low bound on Y_i may be set corresponding to the primordial big bang nucleosynthesis value (e.g. Silva Aguirre et al. 2015, 2017; Li et al. 2020; Valle et al. 2020). The former is known to yield optimal model solutions inferred using forward modelling techniques[4] having initial helium values that in some cases are below the primordial big bang nucleosynthesis value. (e.g. Bonaca et al. 2012; Lebreton & Goupil 2014; Metcalfe et al. 2014; Silva Aguirre et al. 2015, 2017). This option of determining Y_i leads to an increase in the number of stellar grid variable parameters, thus it is costly in terms of the computational time and storage capacity for the computed models.

The helium enrichment law in equation (1) is commonly employed in stellar model grid construction, however, a major setback in using equation (1) is that no consensus has yet been reached regarding the value of the helium-to-heavy element ratio. Based on the observation of K dwarf stars in the *Hipparcos* catalogue, Jimenez et al. (2003) reported the $\Delta Y/\Delta Z$ value to be 2.1 ± 0.4. These results are in agreement with those obtained based on a set of Padova isochrones constructed with a wide range of helium and metal content to fit observations of nearby K dwarf stars, that is, $\Delta Y/\Delta Z = 2.1 \pm 0.9$ (Casagrande et al. 2007). Exploring the metal-poor galaxy H II regions, Magellanic Cloud H II regions, and M17 abundances while taking into account the effects of temperature fluctuations, Balser (2006) reported the value of $\Delta Y/\Delta Z$ to be 1.6. Interestingly, when using only galaxy H II region S206 and M17, Balser (2006) determines $\Delta Y/\Delta Z = 1.41 \pm 0.62$, a value reported to be consistent with that from standard chemical evolution models. Serenelli & Basu (2010) reported the helium-to-heavy element enrichment ratio of the Sun to vary in the range $1.7 \leq \Delta Y/\Delta Z \leq 2.2$ depending on the choice of solar composition. Through the analysis of glitch signatures caused by the ionization of helium in 38 *Kepler* 'LEGACY' sample stars, Verma et al. (2019) estimated their surface helium abundances. Combining these values with abundance differences caused by gravitational settling in stellar models, they estimated the initial helium abundances and derived a primordial helium abundance of 0.244 ± 0.019 with $\Delta Y/\Delta Z = 1.226 \pm 0.843$. In sum, the acceptable values of the helium-to-heavy enrichment ratio span the interval $1 \leq \Delta Y/\Delta Z \leq 3$, notwithstanding lower values being found in some cases, especially when one determines the value of $\Delta Y/\Delta Z$ based on solar calibrations. Furthermore, through exploring the relations between Y and Z in the interstellar medium of simulated disc galaxies, Vincenzo et al. (2019) report that $\Delta Y/\Delta Z$ is not constant and evolves as a function of time, depending on the specific chemical element chosen to trace Z.

Given the fact that the helium abundance affects the structure and evolution lifetime of stars, this implies that any uncertainties in helium abundance directly impacts on the determination of the stellar parameters such as, radius, mass, and age. Therefore, the treatment of the initial helium abundance in stellar models is a substantial source of systematic uncertainties on stellar properties derived using forward modelling techniques. Lebreton & Goupil (2014) carried out a detailed characterization of the *COROT* exoplanet host HD 52265 and reported a scatter of about 5 per cent in mass arising from the treatment of initial helium mass fraction. Using synthetic data for about 10 000 artificial stars, Valle et al. (2014) found the systematic bias on mass and radius estimation arising from a variation of ± 1 in $\Delta Y/\Delta Z$ to be 2.3 per cent and 1.1 per cent, respectively. Further, Valle et al. (2015) reported the systematic bias in age to be about one-fourth of the statistical error in the first 30 per cent of the evolution, while its negligible for more evolved stars.

In this article, we perform a detailed study of a sample of low-mass main-sequence stars with high signal-to-noise asteroseismic data from multiyear *Kepler* photometry (Lund et al. 2017), making asteroseismic inferences to quantify the systematic uncertainties on the derived stellar global parameters (i.e. mean density, radius, mass, and age) arising from the treatment of initial helium abundance in stellar grids. In addition, we assess if these systematic uncertainties are within the ESA's PLATO (PLAnetary Transits and Oscillations of stars; Rauer et al. 2014) mission accuracy requirements for exoplanet-host star properties, needed for precise planet characterization.

This article is organized as follows. In Section 2, we describe our target sample, the details of the stellar grids, and optimization routines employed. In Section 3, we present our results and discussions, while Section 4 contains our conclusions.

2 TARGET SAMPLE AND STELLAR MODELS

The seismic and atmospheric observations used for our target sample are described in Section 2.1, while Section 2.2 is composed of a description of the stellar grids and best-fitting model selection procedures employed in the forward modelling routines.

2.1 *Kepler* data

The location of the *Kepler* LEGACY sample stars employed in this study is shown in the asteroseismic Hertzsprung–Russel diagram (see Fig. 1). The y-axis of Fig. 1 contains the values of the average large separations, $\Delta\nu$, adopted from Lund et al. (2017). These were estimated in that work using as a linear fit to the spherical mode degree $l = 0$ frequencies expressed as a function of the radial order, n.

The sample shown in Fig. 1 consists of 35 low-mass solar-type stars with at least 12 months observation of short cadence data ($\Delta t = 58.89$ s). The seismic data of these stars are available in Lund et al. (2017). It is worth noting that for each star, we only adopted oscillation modes whose probability of detection is reported to be at least '*strong*' by Lund et al. (2017). Refer to equation (15) in Lund et al. (2017) for details on the probability of the detection of the given set of modes. Table 1 shows the values of spectroscopic parameters, that is, metallicity, [Fe/H], and effective temperatures, $T_{\rm eff}$, for each star in our sample. Our stellar sample also includes the asteroseismic

[4]Forward modelling involves determining fundamental stellar parameters by matching model parameters to the observed properties, for example, seismic observables (such as individual oscillation frequencies or frequency ratios) and non seismic observables (effective temperature, metallicity, and luminosity).

Downloaded from https://academic.oup.com/mnras/article/500/1/54/5925370 by Inst. Astrofisica Andalucia CSIC user on 10 February 2021

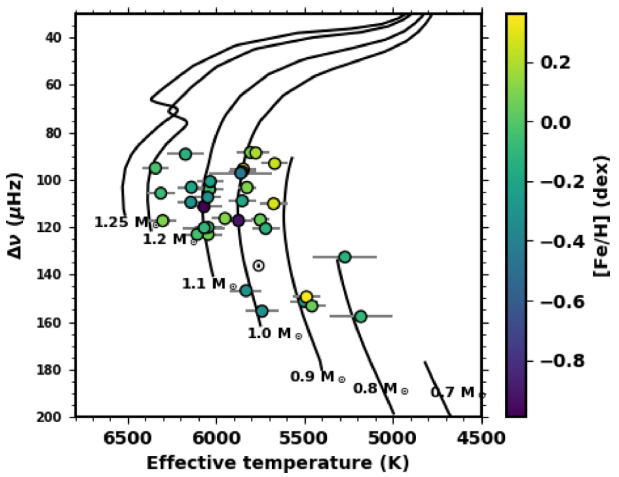

Figure 1. Asteroseismic Hertzsprung–Russell diagram showing the parameter space covered by 35 low-mass LEGACY sample stars. Circles: target stars colour coded according to their respective metallicities. Black lines: stellar evolutionary tracks ranging in mass from 0.7 to 1.25 $M_{\odot}$ constructed using a mixing length parameter (α_{mlt}) of 1.8 in order to describe convection, a heavy metal mass fraction (Z) of 0.02, and an initial helium mass fraction was obtained using equation (1), with $\Delta Y/\Delta Z$ set to 1.4.

binary HD 176465 (White et al. 2017; Nsamba et al. 2017) and the Sun, whose average large frequency separation and spectroscopic parameters are shown in Table 2.

2.2 Stellar models and optimization

We constructed three stellar grids (namely; A, B, and C) varying only in the treatment of the initial helium mass fraction (Y_i), using MESA version 9793. The evolutionary tracks were evolved from the pre-main sequence (PMS) and stellar models were stored starting from the zero-age main-sequence (ZAMS) which we defined as the region along the evolutionary tracks where the model nuclear luminosity is approximately 99 per cent of its total luminosity. Two termination criteria were specified during the grid construction, that is, evolutionary tracks were terminated when: (i) models reach a stellar age of 16 Gyr. This explains why the evolutionary tracks with stellar masses of 0.7, 0.8, and 0.9 $M_{\odot}$ shown in Fig. 1 do not reach the subgiant stage. (ii) They reach a region along the evolutionary track where $\log\rho_c = 4.5$ (ρ_c is the model central density). The model selection along the evolution tracks was based on a variation in the central hydrogen abundance of ~ 0.007.

Table 3 provides a summary of different grid constituents. The stellar evolutionary tracks in all the grids were varied in mass, $M \in [0.7–1.25]$ $M_{\odot}$ in steps of 0.05 $M_{\odot}$, $Z \in [0.004$ to $-0.04]$ in steps of 0.002, and $\alpha_{mlt} \in [1.2–3.0]$ in steps of 0.2. In grid A, the initial helium abundance, $Y_i \in [0.22 - 0.32]$ in steps of 0.02. Diffusion of hydrogen and gravitational settling of heavy elements without radiative acceleration was included in all our stellar grids as indicated in Table 3 following the description of Thoul, Bahcall & Loeb (1994). We note that element diffusion has been reported to be an efficient transport process in low-mass stars (e.g. Théado et al. 2005; Valle et al. 2015; Higl & Weiss 2017; Nsamba et al. 2018a). Furthermore, radiative acceleration is reported to have a negligible impact in stars within the same mass range as the Sun, that is, below 1.2 $M_{\odot}$. This is because radiative acceleration is systematically weak compared to gravitational settling or gravity in such stars (Turcotte et al. 1998; Deal et al. 2017, 2018).

Table 1. Global asteroseismic and spectroscopic parameters of our stellar sample.

KIC	$\Delta\nu$ (μ Hz)	T_{eff} (K)	[Fe/H] (dex)	Ref.
3427720	$120.068^{+0.031}_{-0.032}$	6045 ± 77	-0.06 ± 0.10	1
3656476	$93.194^{+0.018}_{-0.020}$	5668 ± 77	0.25 ± 0.10	1
3735871	$123.049^{+0.047}_{-0.046}$	6107 ± 77	-0.04 ± 0.10	1
4914923	$88.531^{+0.019}_{-0.019}$	5805 ± 77	0.08 ± 0.10	1
5184732	$95.545^{+0.024}_{-0.023}$	5846 ± 77	0.36 ± 0.10	1
5950854	$96.629^{+0.102}_{-0.107}$	5853 ± 77	-0.23 ± 0.10	1
6106415	$104.074^{+0.023}_{-0.026}$	6037 ± 77	-0.04 ± 0.10	1
6116048	$100.754^{+0.017}_{-0.017}$	6033 ± 77	-0.23 ± 0.10	1
6225718	$105.695^{+0.018}_{-0.017}$	6313 ± 77	-0.07 ± 0.10	1
6603624	$110.128^{+0.012}_{-0.012}$	5674 ± 77	0.28 ± 0.10	1
7106245	$111.376^{+0.063}_{-0.061}$	6068 ± 102	-0.99 ± 0.19	2
7296438	$88.698^{+0.040}_{-0.036}$	5775 ± 77	0.19 ± 0.10	1
7871531	$151.329^{+0.025}_{-0.023}$	5501 ± 77	-0.26 ± 0.10	1
8006161	$149.427^{+0.015}_{-0.014}$	5488 ± 77	0.34 ± 0.10	1
8150065	$89.264^{+0.134}_{-0.121}$	6173 ± 101	-0.13 ± 0.15	2
8179536	$95.090^{+0.058}_{-0.054}$	6343 ± 77	-0.03 ± 0.10	1
8379927	$120.288^{+0.017}_{-0.018}$	6067 ± 120	-0.10 ± 0.15	3
8394589	$109.488^{+0.034}_{-0.035}$	6143 ± 77	-0.29 ± 0.10	1
8424992	$120.584^{+0.062}_{-0.064}$	5719 ± 77	-0.12 ± 0.10	1
8760414	$117.230^{+0.022}_{-0.018}$	5873 ± 77	-0.92 ± 0.10	1
9025370	$132.628^{+0.030}_{-0.024}$	5270 ± 180	-0.12 ± 0.18	4
9098294	$108.894^{+0.023}_{-0.022}$	5852 ± 77	-0.18 ± 0.10	1
9139151	$117.294^{+0.031}_{-0.032}$	6302 ± 77	0.10 ± 0.10	1
9410862	$107.390^{+0.050}_{-0.053}$	6047 ± 77	-0.31 ± 0.10	1
9955598	$153.283^{+0.029}_{-0.032}$	5457 ± 77	0.05 ± 0.10	1
9965715	$97.236^{+0.041}_{-0.042}$	5860 ± 180	-0.44 ± 0.18	4
10079226	$116.345^{+0.059}_{-0.052}$	5949 ± 77	0.11 ± 0.10	1
10644253	$123.080^{+0.056}_{-0.055}$	6045 ± 77	0.06 ± 0.10	1
10963065	$103.179^{+0.027}_{-0.027}$	6140 ± 77	-0.19 ± 0.10	1
11772920	$157.746^{+0.032}_{-0.033}$	5180 ± 180	-0.09 ± 0.18	4
12069424	$103.277^{+0.021}_{-0.020}$	5825 ± 50	0.10 ± 0.03	5
12069449	$116.929^{+0.012}_{-0.013}$	5750 ± 50	0.05 ± 0.02	5

Notes. All values of the average large frequency separation are adopted from Lund et al. (2017). The fourth column shows the source of the spectroscopic parameters, that is, (1) Buchhave & Latham (2015), (2) Casagrande et al. (2014), (3) Pinsonneault et al. (2012), (4) Pinsonneault et al. (2014), and (5) Ramírez, Meléndez & Asplund (2009).

Table 2. Global asteroseismic and spectroscopic parameters of the asteroseismic binary HD 176465 and the Sun.

Star name	$\Delta\nu$ (μ Hz)	T_{eff} (K)	[Fe/H] (dex)
HD 176465 A	146.79 ± 0.12	5830 ± 90	-0.30 ± 0.06
HD 176465 B	155.42 ± 0.13	5740 ± 90	-0.30 ± 0.06
Sun	138.8 ± 0.10	5777 ± 65	0.00 ± 0.05

Notes. All parameters for the binary HD 176465 are adopted from White et al. (2017). The solar average large frequency separation is obtained from Mosser et al. (2013), while the effective temperature and metallicity are from Malagnini & Morossi (1997).

Downloaded from https://academic.oup.com/mnras/article/500/1/54/5925370 by Inst. Astrofisica Andalucia CSIC user on 10 February 2021

Table 3. Stellar grid constituents.

Grid name	Mass ($M_\odot$)	Diffusion	Overshoot	$\Delta Y / \Delta Z$
A	0.7 – 1.25	Yes	No	...
B	0.7 – 1.25	Yes	No	1.4
C	0.7 – 1.25	Yes	No	2.0

The general input physics used in all the grids include nuclear reaction rates obtained from JINA REACLIB (Joint Institute for Nuclear Astrophysics Reaction Library; Cyburt et al. 2003) version 2.2 with specific rates for $^{12}C(\alpha,\gamma)^{16}O$ and $^{14}N(p,\gamma)^{15}O$ described by Kunz et al. (2002) and Imbriani et al. (2005), respectively. At high temperatures, OPAL tables (Iglesias & Rogers 1996) were used to cater for opacities while tables from Ferguson et al. (2005) were used at lower temperatures. All the grids used the 2005 updated version of the OPAL equation of state (Rogers & Nayfonov 2002). The surface boundary of stellar models was described using the standard Grey–Eddington atmosphere. This integrates the atmosphere structure from the photosphere down to an optical depth of 10^{-4}. In all the stellar grids, the surface chemical abundances of Grevesse & Sauval (1998) with $Z_\odot$ of 0.0169 were used in the conversions of $[Fe/H] = \log(Z_{surface}/X_{surface})_{star} - \log(Z_{surface}/X_{surface})_\odot$. $X_{surface}$ and $Z_{surface}$ are the surface hydrogen and heavy element mass fractions, respectively.

The adiabatic oscillation frequencies for the spherical mode degrees, $l = 0$, 1, 2, and 3 were calculated using GYRE oscillation code (Townsend & Teitler 2013). Stellar model oscillation frequencies are known to suffer from surface effects which need to be corrected for before being compared to the observed frequencies (see Dziembowski, Paterno & Ventura 1988; Christensen-Dalsgaard & Thompson 1997; Roxburgh & Vorontsov 2003). A number of empirical expressions have been suggested to handle these offsets based on the assumption that they follow a known functional form (Kjeldsen, Bedding & Christensen-Dalsgaard 2008; Ball & Gizon 2014; Sonoi et al. 2015) and their impact on the inferred stellar parameters explored (Ball & Gizon 2017; Nsamba et al. 2018a; Basu & Kinnane 2018; Jørgensen et al. 2020). We use the two-term surface correction suggested by Ball & Gizon (2014) because it was found to yield the least systematic uncertainties on the derived stellar parameters of main-sequence stars. The proposed empirical expression describing the frequency difference ($\delta\nu$) takes the form

$$\delta\nu = I^{-1}\left[a\left(\frac{\nu}{\nu_{ac}}\right)^{-1} + b\left(\frac{\nu}{\nu_{ac}}\right)^{3}\right], \tag{2}$$

where ν_{ac} is the acoustic cut-off frequency that scales linearly with ν_{max}, which is suggested to scale as the stellar surface gravity, g, and effective temperature, T_{eff}, that is, $\nu_{ac} \propto \nu_{max} \propto g T_{eff}^{-1/2}$ (Brown et al. 1991; Kjeldsen & Bedding 1995). I is the mode inertia, a and b are free parameters.

We employ AIMS (Asteroseismic Inference on a Massive Scale; Rendle et al. 2019), an optimization tool based on a Bayesian routine and Markov Chain Monte Carlo (MCMC) approach so as to explore the model parameter space and find models having parameters comparable to the specified sets of classical and seismic observables. It is essential to note that we specified equal weights to both classical and seismic observables, thus the total χ^2_{total} is expressed as

$$\chi^2_{total} = \left(\frac{N_{classical}}{N_{seismic}}\right)\chi^2_{seismic} + \chi^2_{classical}, \tag{3}$$

where $N_{seismic}$ is the number of seismic observables and $N_{classical}$ is the number of classical observables,

$$\chi^2_{seismic} = \sum_i^N \left(\frac{\nu_i^{(obs)} - \nu_i^{(mod)}}{\sigma(\nu_i)}\right)^2,$$

$$\chi^2_{classical} = \left(\frac{T_{eff}^{(obs)} - T_{eff}^{(mod)}}{\sigma(T_{eff})}\right)^2 + \left(\frac{[Fe/H]^{(obs)} - [Fe/H]^{(mod)}}{\sigma([Fe/H])}\right)^2, \text{ and}$$

$\nu_i^{(obs)}$ and $\nu_i^{(mod)}$ are the observed and model frequencies, respectively. Although the weight on each observable should be the same from the statistical point of view, in practice it has been noted that giving similar weights to each observation, thus decreasing the relative impact of the classical constraints in the fit, often leads to results that are biased, possibly due to inaccuracies in the models. This matter has been assessed in the context of a recent hare and hound exercise for PLATO (Cunha et al., in preparation). In this article, we aimed at avoiding that possible bias. While this choice results in larger uncertainties in the parameters estimated from the fit, compared to those found when each observable is given the same weight, the results are expected to be more accurate.

Finally, the stellar parameters and their corresponding uncertainties are obtained as the mean and standard derivation of the posterior distributions. The relative differences ($\Delta\phi/\phi_b$) between stellar parameters from different grids is determined using the expression

$$\frac{\Delta\phi}{\phi} = \left(\frac{\phi_a - \phi_b}{\phi_b}\right), \tag{4}$$

where ϕ is any stellar parameter (e.g. mass, M, radius, R, density, ρ, initial helium abundance, Y_i, age, t, etc.), and ϕ_a and ϕ_b are the inferred stellar parameters from grid a and b.

3 RESULTS AND DISCUSSION

In Section 3.1, we compare the results from grids B and C, considering grid B as the reference grid. We also quantify the associated systematic uncertainties arising from the difference in the treatment of initial helium abundance in both grids. A similar comparison is made in Section 3.2 between grids A and B, and A and C, taking grid A as the reference grid. Section 3.3 contains solar parameters derived from the different grids and a comparison between the surface helium abundances from grid A and those estimated using glitch analysis approach.

3.1 Comparison between grids B and C

We note that grids B and C vary only in the value of the helium-to-heavy element ratio (see Table 3) used in equation (1). The stellar masses from grid C computed with a higher helium-to-heavy element ratio compared to that used in grid B yields lower masses as shown in the top left panel of Fig. 2. This is also illustrated by a bias (μ) ~ -0.028. Assuming a fully ionized gas mixture, the mean molecular weight is defined as (e.g. Kippenhahn, Weigert & Weiss 2012);

$$\mu_g = \frac{4}{6X + Y + 2}, \tag{5}$$

and also considering the definition (e.g. Kippenhahn et al. 2012);

$$\mu_g = \frac{\bar{m}}{m_H}, \tag{6}$$

where $\bar{m}$ is the average mass of the particles (atoms, ions, or molecules) in the gas, m_H is the mass of hydrogen assuming an hydrogen gas.

Downloaded from https://academic.oup.com/mnras/article/500/1/54/5925370 by Inst. Astrofisica Andalucia CSIC user on 10 February 2021

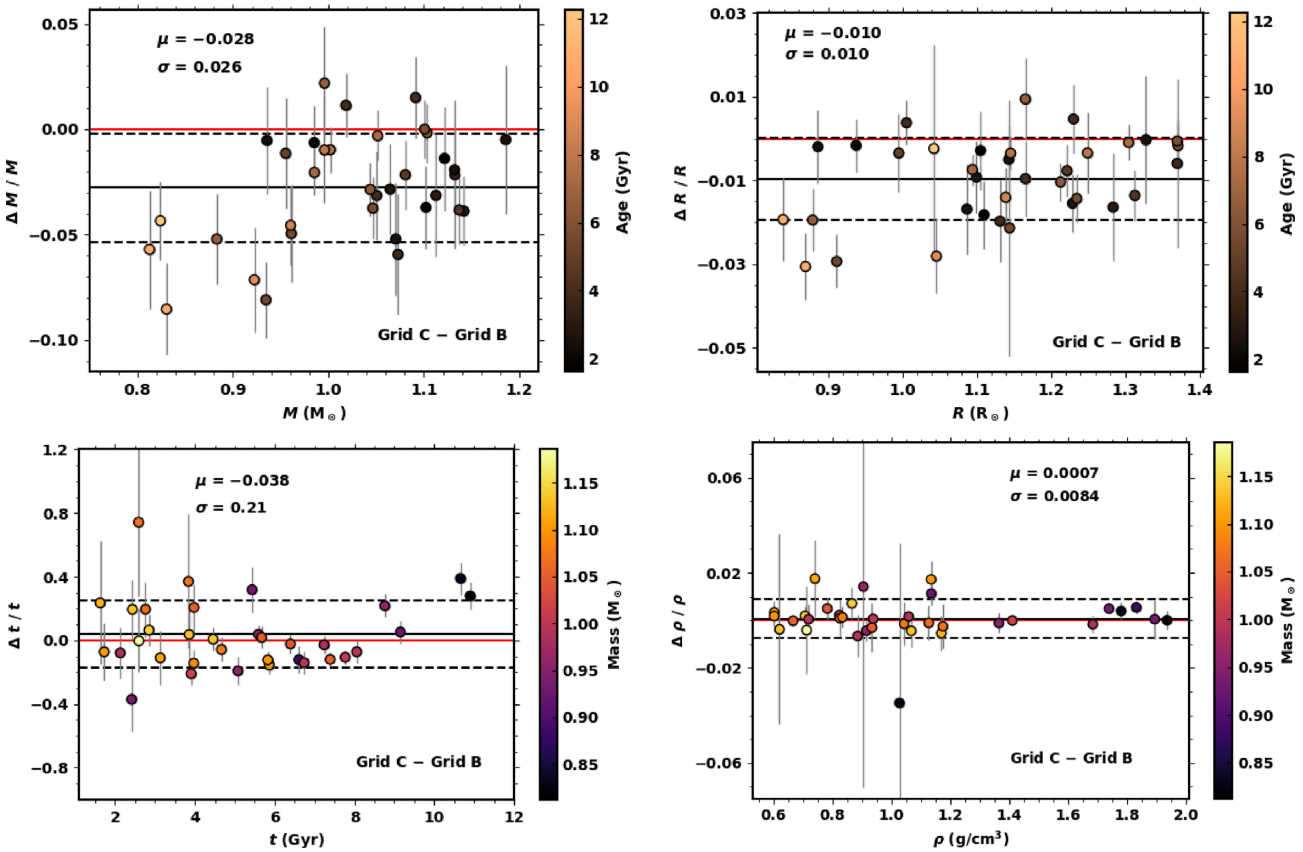

Figure 2. Grid C versus grid B: fractional difference in mass (top left), radius (top right), age (bottom right), and mean density (bottom right) as a function of stellar parameters from grid B. The colour-coding is with respect to stellar age (for both top panels) and stellar mass (for both bottom panels). The solid black line indicates the bias (μ), while the scatter (σ) is represented by the dashed lines. The zero level is represented by the solid red line.

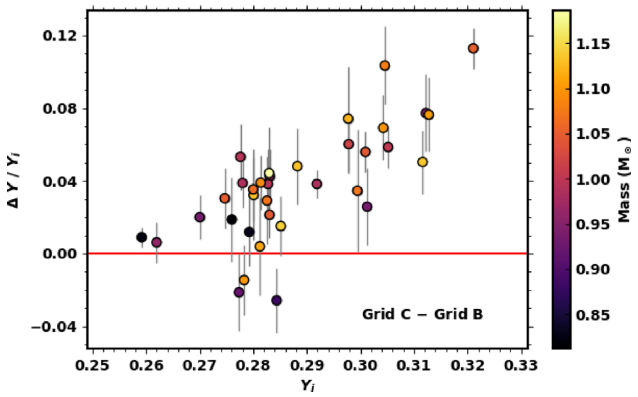

Figure 3. Fractional difference in initial helium abundance as a function of initial helium abundance from grid B. The colour-coding is with respect to stellar mass. The zero level is represented by the solid red line.

For a given set of Z values, larger values of Y in grid C are associated with a larger value of $\Delta Y/\Delta Z$ employed in equation (1) compared to that used in grid B (see Fig. 3). Considering the constraint $X + Y + Z = 1$ and for a fixed Z, increase in Y leads to increase in the μ_g (see equations 5 and 6), which in turn increases the rate of energy production since more nuclear reactions are taking place per unit time due to the increase in central temperature, that is, $T_c \propto \mu_g$. This yields higher luminosity and effective temperature. However, in order to prevent this increase in luminosity, which is indirectly constrained using the effective temperature (part of the classical constraints) and seismic data via the Stefan–Boltzmann's relation (e.g. Boltzmann 1884; Paul et al. 2015; Montambaux 2018), grid C yields optimal model solutions with lower masses and radii (see both top panels of Fig. 2) compared to grid B so as to satisfy the required effective temperature and luminosity. The left bottom panel of Fig. 2 shows a relatively good agreement between ages from both grids B and C with an expected correlation with mass, that is, high-mass stars are younger compared to low-mass stars. However, a large scatter of ~ 21 per cent between the ages can be noted.

We note that both grids B and C yield stellar mean densities which are in good agreement, with a bias of ~ 0.07 per cent and a scatter of ~ 0.84 per cent (see bottom right panel of Fig. 2). This is expected since we used the same set of individual oscillation frequencies which contain information of the stellar mean density (e.g. Ulrich 1986; Aerts, Christensen-Dalsgaard & Kurtz 2010; Belkacem et al. 2013; Suárez et al. 2014).

3.2 Comparison between grids A and B, and A and C

We now address the impact of using free initial helium abundance values (i.e. as carried out in grid A) on the inferred stellar parameters. Fig. 4 shows a scatter of the preferred initial helium abundance values for the optimal model solutions of our stellar sample. It is evident that this scatter does not suggest any relation between initial helium abundance and initial metal abundance. In fact, using MCMC while taking into consideration the associated errors on the initial helium abundance values, we find a slope of $\Delta Y/\Delta Z = 0.827^{+0.345}_{-0.344}$

Downloaded from https://academic.oup.com/mnras/article/500/1/54/5925370 by Inst. Astrofisica Andalucia CSIC user on 10 February 2021

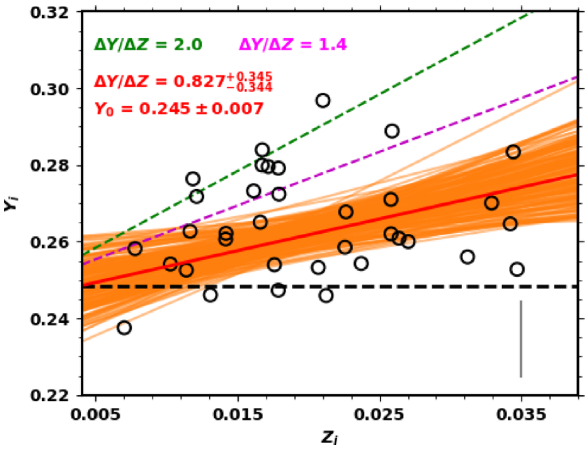

Figure 4. Initial helium abundance as a function of initial heavy elements abundance from grid A which does not constrain the chemical composition with the helium-to-heavy element ratio. The horizontal black dashed line shows the primordial helium abundance from Cyburt et al. (2003). The green and magenta dashed lines correspond to the helium-to-heavy element ratios used in grids C and B, respectively. The red solid line correspond to a fit obtained using MCMC, characterized by a slope and intercept shown in red on the panel. The orange band around the red solid line corresponds to the Monte Carlo regression uncertainty. The vertical grey line represents the average error on the initial helium abundance values. The median uncertainty on the initial metal mass fraction abundance is 0.002.

and $Y_0 = 0.245 \pm 0.007$. This $\Delta Y/\Delta Z$ value is lower than those based on observations, that is, employed in grids B and C (also see Introduction). This is consistent with some literature findings, for example, Silva Aguirre et al. (2015, 2017). The $Y_0 = 0.245 \pm 0.007$ is also consistent with that suggested by Cyburt et al. (2003), that is, $0.2484^{+0.0004}_{-0.0005}$. One would then ask, why do we continue to use equation (1) to determine the model initial helium abundance?. This is mainly because observations suggest a $\Delta Y/\Delta Z$ ratio value (e.g. Jimenez et al. 2003; Balser 2006; Casagrande et al. 2007) and also implementing equation (1) reduces the grid parameter space and is therefore computationally less expensive. We suggest that a single value of $\Delta Y/\Delta Z$ can be used to describe globally and on average the Y enrichment in relation to Z for a sample of stars, but not from star-to-star (in particularly when describing population I stars).

In this context, it is important to understand how the inferred stellar parameters differ when grids with a constant $\Delta Y/\Delta Z$ ratio and grids with free initial helium abundance are employed. The top left panels of Figs 5 and 7 show the relative fractional differences in mass when grid A is compared to grids C and B, respectively. Over all, grids C and B yield lower masses compared to grid A with a scatter of 4.1 per cent and 4.9 per cent, and a bias of -3.2 per cent and −0.4 per cent, respectively. Furthermore, the top left panel of Fig. 7 shows that a handful of stars with masses below ~ 0.9 M$_\odot$ from grid B have higher masses compared to those from grid A. Similar results are seen in radius, that is, top right panels of Figs 5 and 7 with a scatter of 1.6 per cent and 1.8 per cent, respectively. The systematic uncertainties on mass are consistent with findings of Lebreton & Goupil (2014) who reported a scatter of ~ 5 per cent in mass arising from the treatment of initial helium mass fraction when characterizing the *COROT* exoplanet-host HD 52265. We note that HD 52265 has a mass slightly higher than that of our stellar sample, that is, in the range [1.14–1.32] M$_\odot$. The left- and right-hand panels of Fig. 6 show that the optimal models from grid A generally have lower initial helium abundances compared to optimal models from grids C and B, respectively. This may in part be the origin of the differences observed in mass and radius as discussed in Section 3.1. An excellent agreement in the mean density is shown in the right bottom panels of Figs 5 and 7 with a scatter of ~ 0.9 per cent. Despite the low biases in stellar ages (see bottom left panels of of Figs 5 and 7), we report significant systematic uncertainties in stellar ages of upto ~ 29 per cent.

To understand how relevant these systematic uncertainties are, we compare them to the statistical uncertainties in Fig. 8. We note that only a comparison between grids A and C is shown. This is because the systematics between grids A and C are commensurate with those between grids A and B. However, it is worth noting that significant biases in mass and radius exist as shown in Figs 5 and 7. The left bottom panel of Fig. 8 shows that systematic uncertainties in age are greater than statistical uncertainties, highlighting the need for these to be accounted for during model parameter comparisons if a grid with fixed $\Delta Y/\Delta Z$ value is considered. Fig. 8 also shows a comparison between the systematic uncertainties and the ESA's PLATO accuracy requirements for stellar parameters of exoplanet host. It is interesting to report that the treatment of initial helium abundance in stellar model grids yields masses and radii within the expected PLATO accuracy limits, that is, 2–4 per cent for the radius and 10–15 per cent for the mass of the exoplanet host (Rauer et al. 2014). The left bottom panel of Fig. 8 shows that variations in the treatment of the initial helium abundance yield larger systematic uncertainties on stellar age compared to the required PLATO exoplanet-host accuracy age limits, that is, 10 per cent on ages (Rauer et al. 2014).

3.3 Solar parameters and surface helium abundances using acoustic glitches

In order to test how well these different grids reproduce the Sun as a star, we obtained a set of frequencies from Lund et al. (2017) which are determined from solar data degraded in quality to match that of the *Kepler* mission. Table 4 shows that grids B and C reproduce the mass and radius of the Sun within 1σ error, while grid A recovers the solar mass and radius within 1.5σ. All the grids yield the solar mean density within 1σ. Grids A and B yield the expected solar age within 1σ error but grid C yields a lower age value. Since all our grids employ chemical abundances from Grevesse & Sauval (1998), the element mass fraction abundances for this mixture are $X = 0.735$, $Y = 0.248$, and $Z = 0.017$, with $Z/X = 0.023$. These are only satisfied within 1σ error by results from grid A (see Table 4 and Fig. 9). We also note that the solar surface helium abundance from grid A is consistent with the helioseismic value. Therefore, we consider stellar parameters derived using grid A to be more accurate than those from grids B and C. The solar reference values considered in Fig. 9 are; mass, $M = 1$ M$_\odot$ (e.g. Prša et al. 2016), radius, $R = 1$ R$_\odot$ (Allen 1976; Emilio et al. 2012), density, $\rho = 1.410$ g cm^{-3}, age, $t = 4.57 \pm 0.42$ Gyr (e.g. Connelly et al. 2012), surface helium mass fraction, $Y_s = 0.248$ (Basu & Antia 2004), and metal mass fraction, $Z_s = 0.017$ (Grevesse & Sauval 1998).

The surface (or envelope) helium abundance (Y_s) can be determined using a '*semidirect*' approach involving the analysis of a short scale structural variation associated to the helium ionization zones (Gough & Thompson 1988; Gough 1990). This is known as the 'helium glitch'. The helium glitch induces a local change in the first adiabatic index, Γ_1, which creates a variation in the adiabatic sound speed. This in turn creates a signature in the oscillation frequencies and has been observed in the Sun (e.g. Monteiro & Thompson 2005; Houdek & Gough 2007), main-sequence stars (Mazumdar et al. 2014; Verma et al. 2014; Verma et al. 2017), and red giant stars

Downloaded from https://academic.oup.com/mnras/article/500/1/54/5925370 by Inst. Astrofisica Andalucia CSIC user on 10 February 2021

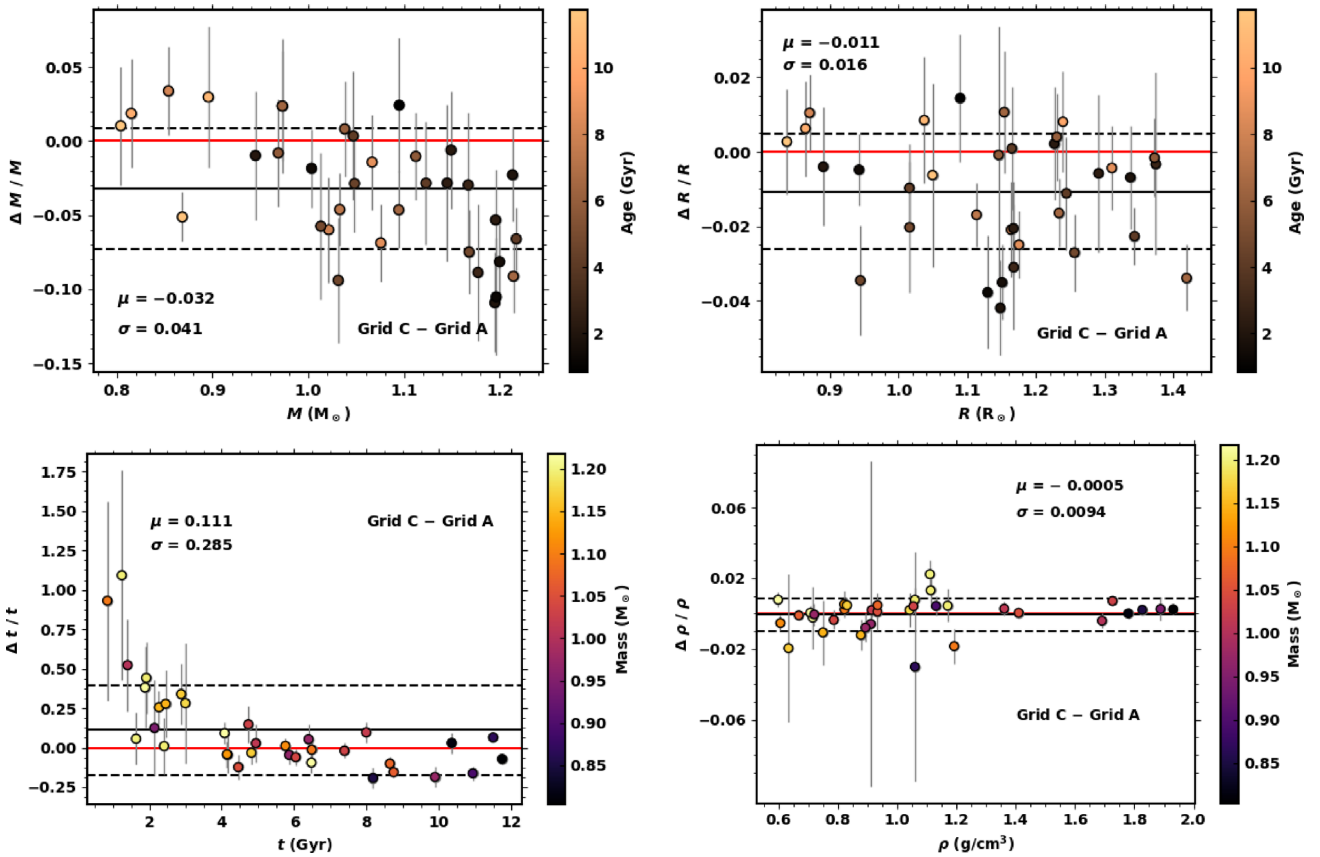

Figure 5. Grid C versus grid A: fractional difference in mass (top left), radius (top right), age (bottom right), and mean density (bottom right) as a function of stellar parameters from grid A. The colour-coding is with respect to stellar age (for both top panels) and stellar mass (for both bottom panels). The solid black line indicates the bias (μ), while the scatter (σ) is represented by the dashed lines. The zero level is represented by the solid red line.

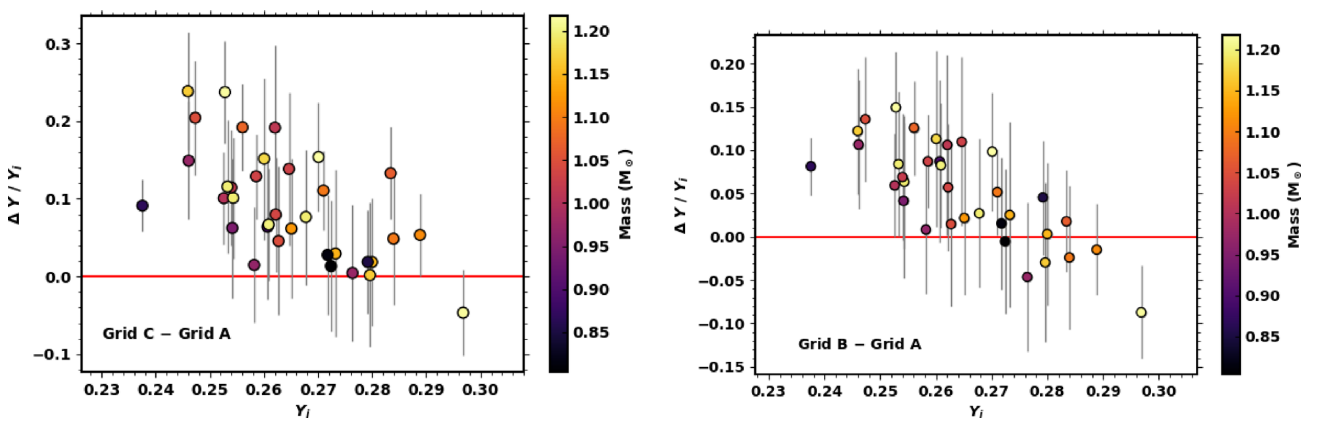

Figure 6. Fractional difference in initial helium abundance as a function of initial helium abundance from A. Left-hand panel: comparison between grids C and A. Right-hand panel: comparison between grids B and A. The colour-coding is with respect to stellar mass from grid A. The zero level is represented by the solid red line.

(e.g. Miglio et al. 2010; Broomhall et al. 2014; Vrard et al. 2015; Corsaro, De Ridder & García 2015; Dréau et al. 2020). Table 5 shows a comparison of the surface helium abundances of the binary stars in our sample and those in Verma et al. (2014, 2019). The surface helium abundances from Verma et al. (2014, 2019) are based on glitch analysis. The surface helium abundance values for the best-fitting models of 16 Cyg A, KIC 6106415, and KIC 6116048 from grid A agree within 1σ (see Table 5) with those from Verma et al. (2014, 2019). Our results for 16 Cyg B agree with those of Verma et al. (2014, 2019) within 1σ and 2σ, respectively.

Verma et al. (2019) selected 38 stars from the LEGACY sample, for which the determination of the surface helium abundances using glitch analysis was possible. Of the 38 stars, 19 of them are part of our sample. Fig. 10 shows a comparison between the surface

Downloaded from https://academic.oup.com/mnras/article/500/1/54/5925370 by Inst. Astrofisica Andalucia CSIC user on 10 February 2021

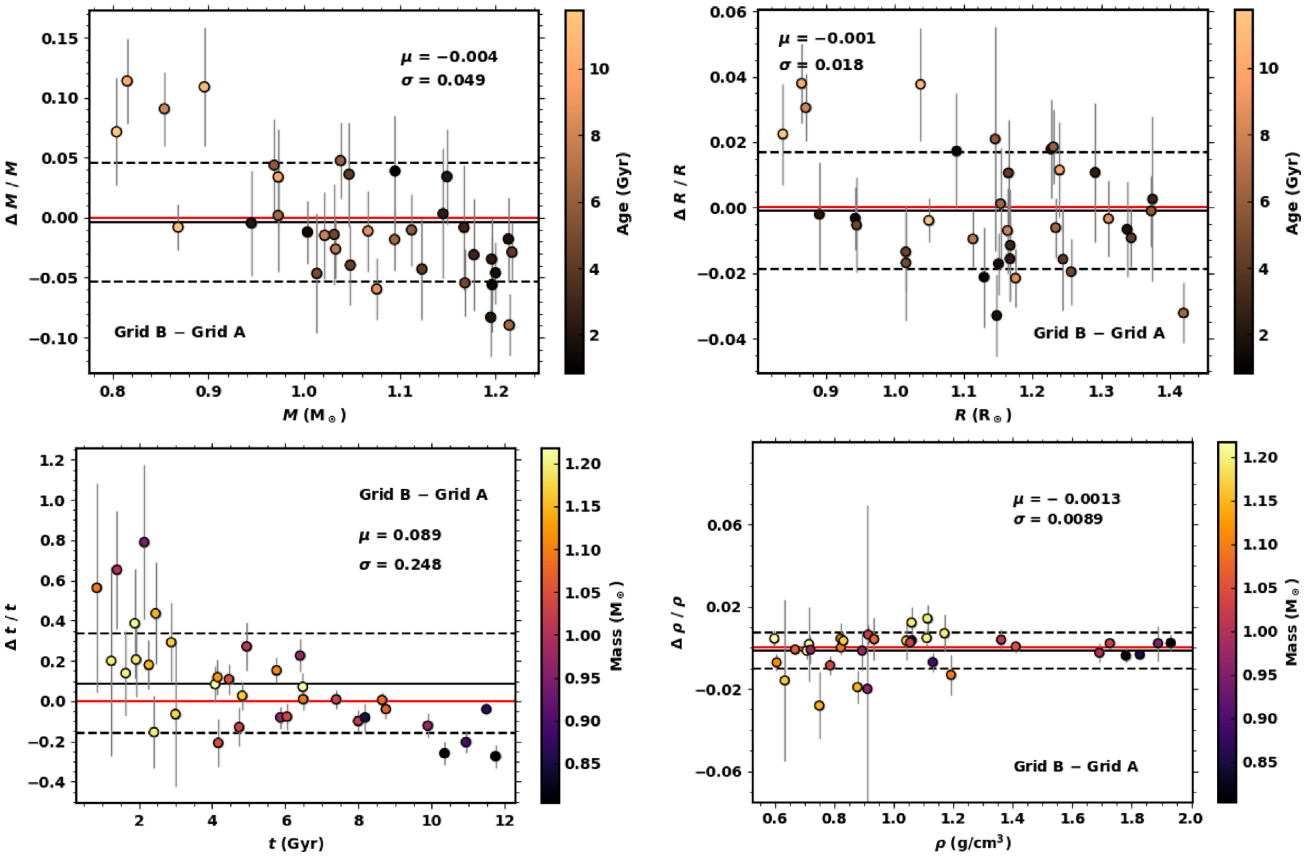

Figure 7. Grid B versus grid A: fractional difference in mass (top left), radius (top right), age (bottom right), and mean density (bottom right) as a function of stellar parameters from grid A. The colour-coding is with respect to stellar age (for both top panels) and stellar mass (for both bottom panels). The solid black line indicates the bias (μ), while the scatter (σ) is represented by the dashed lines. The zero level is represented by the solid red line.

helium abundances of the best-fitting models of grid A for these stars and those determined based on glitch analysis, while employing calibration models generated using MESA in Verma et al. (2019). The surface helium abundances agree within 1σ–2σ. We note that the glitch analysis approach is not completely model independent since it relies on calibration models (see Verma et al. 2014, 2019 for details). Therefore, the offset in Y_s of about -0.012 (see Fig. 10) for most of the stars may be attributed to the differences in the model physics employed in the calibration models used in Verma et al. (2019) and our grid A models. A vital difference lies in the opacities adopted. The MESA models of Verma et al. (2019) were generated using opacity tables from the Opacity Project (OP, Badnell et al. 2005; Seaton 2005; Ferguson et al. 2005) while our grid A contains models calculated using OPAL opacity tables (Iglesias & Rogers 1996; Ferguson et al. 2005). A change in opacities not only creates differences in the depth of convective envelopes but also creates changes in the inferred surface element abundances (e.g. see Bahcall, Serenelli & Pinsonneault 2004). The impact of the different model physics employed in stellar grids of solar-type stars on the derived parameters has been addressed in Basu & Antia (2004), Silva Aguirre et al. (2015, 2017), Valle et al. (2015), Deal et al. (2017, 2018), Nsamba et al. (2018b, 2019), among others.

4 CONCLUSIONS

In this article, we have used low-mass 'LEGACY' sample stars from *Kepler* to explore the impact and systematic uncertainties on inferred stellar properties arising from the treatment of initial helium abundance in stellar model grids. Our analysis considers different commonly used approaches for the determination of the initial helium abundance in forward modelling routines. In particular, we have addressed the following questions:

(i) What is the impact of adopting different galactic enrichment ratios on stellar parameters (mainly, mean density, radius, mass, and age) inferred using forward modelling routines?

(ii) What kind of systematic uncertainties are induced on the inferred stellar parameters when grids with different galactic enrichment ratios are compared to a grid with helium abundance set as a free parameter?

(iii) How do the statistical uncertainties compare to the systematic uncertainties? Are the systematic uncertainties within the PLATO accuracy requirement limits for exoplanet-host stars?

In sum, our findings indicate that grids constructed with high $\Delta Y/\Delta Z$ yield lower masses and radii compared to grids based on low values of $\Delta Y/\Delta Z$, with systematic uncertainties of $\sim$ 2.6 per cent and $\sim$ 1.0 per cent on mass and radius, respectively. The degeneracy between mass and helium is a long standing problem with predictions that it can be broken if precise stellar luminosities are known (see Silva Aguirre et al. 2015). We tested this and found no differences between the results obtained with and without *Gaia*-based luminosities (Moedas, Nsamba & Clara 2020). This is because the precision on the luminosities for the majority of the stars in our sample is not

Downloaded from https://academic.oup.com/mnras/article/500/1/54/5925370 by Inst. Astrofisica Andalucia CSIC user on 10 February 2021

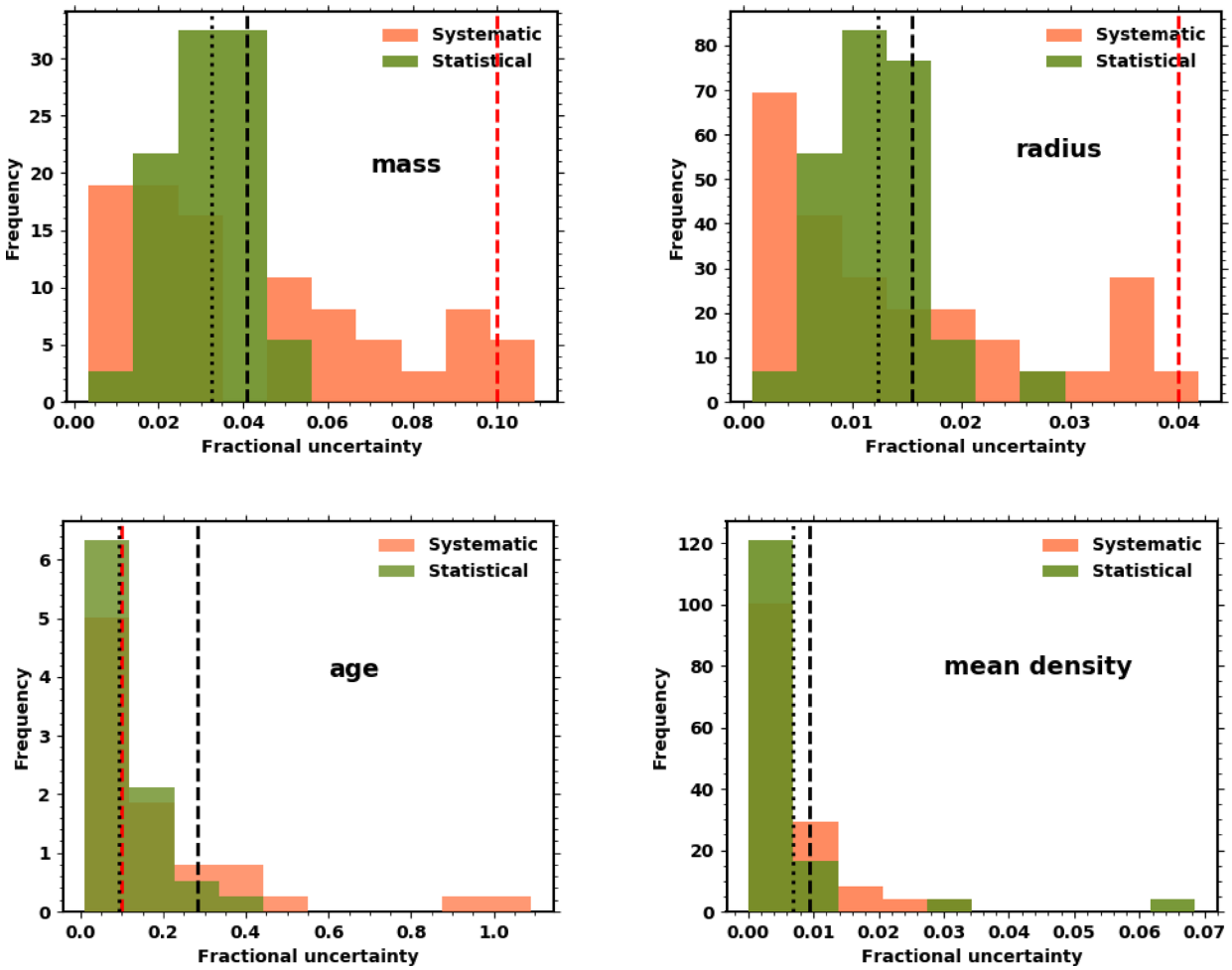

Figure 8. Distributions of statistical uncertainties from grid A (green) and systematic uncertainties from comparing stellar parameters inferred from grids A and C (salmon). Median values are represented by dotted and dashed black lines for the statistical and systematic uncertainty, respectively. The dashed red lines represent the PLATO accuracy requirement limits for stellar parameters (mass, radius, and age) of exoplanet hosts.

Table 4. Parameters of the Sun from the different grids.

Grid	Mass ($M_\odot$)	Radius ($R_\odot$)	Age (Gyr)	Density ($g\,cm^{-3}$)	α_{mlt}	$Y_{surface}$	$Z_{surface}$
A	1.04 ± 0.03	1.015 ± 0.013	4.45 ± 0.25	1.410 ± 0.003	1.97 ± 0.09	0.247 ± 0.015	0.016 ± 0.001
B	1.01 ± 0.01	1.001 ± 0.003	4.91 ± 0.31	1.411 ± 0.003	1.84 ± 0.08	0.256 ± 0.004	0.021 ± 0.002
C	1.02 ± 0.02	1.010 ± 0.004	4.15 ± 0.25	1.410 ± 0.002	1.97 ± 0.09	0.272 ± 0.005	0.023 ± 0.002

sufficient (i.e. median uncertainty ~ 0.5) to add any strong extra constraint on the optimization process.

We also report low initial helium abundance values for the optimal models from the grid with no restrictions set on initial helium abundance, compared to grids which employ an enrichment ratio value (see Fig. 6). This directly impacts on the inferred stellar masses and radii. In addition, we found a handful of stars to have initial helium abundances below the primordial big bang nucleosynthesis value (see Fig. 4). The inference of initial helium abundances below the primordial big bang nucleosynthesis value is not uncommon in forward modelling (e.g. Bonaca et al. 2012; Lebreton & Goupil 2014; Metcalfe et al. 2014; Silva Aguirre et al. 2015, 2017). Mathur et al. (2012) argue that this may indicate a problem with one or more of the observational constraints. This has also been attributed to the choice of solar metallicity mixtures adopted, more specially Asplund et al. (2009) mixtures (see Lebreton & Goupil 2014). Bonaca et al. (2012) demonstrate that in many cases using the solar-calibrated mixing length parameter (α_{mlt}) would lead to estimates of initial helium abundances that are lower than the primordial helium abundance. In this article, we neither use a solar-calibrated mixing length parameter nor Asplund et al. (2009) mixtures, which may explain why the majority of the solutions for our stellar sample lie within the expected initial helium abundance range (see Fig. 4). In fact, given that observations have associated errors, it is expectable that the inferred initially helium abundance may be below the primordial value for a few stars, if stars with low initially helium abundance exist in our

Downloaded from https://academic.oup.com/mnras/article/500/1/54/5925370 by Inst. Astrofisica Andalucia CSIC user on 10 February 2021

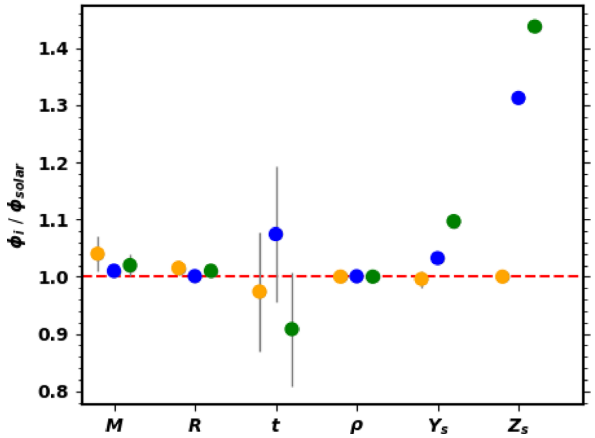

Figure 9. Solar parameters derived using different grids. Parameters from grids A, B, and C are shown in orange, blue, and green, respectively. ϕ_i corresponds to the inferred stellar parameter, that is, mass denoted as M, radius denoted as R, age denoted as t, mean density denoted as ρ, Z_s and Y_s are the surface metal mass fraction and surface helium mass fraction, respectively. ϕ_{solar} denotes the solar parameters. See the text for details.

Table 5. Surface helium abundance of two binary stars in our sample. The second and third columns show surface helium abundances from Verma et al. (2014, 2019), respectively, based on glitch analysis and using a set of calibration models (with diffusion) generated using MESA. The fourth column contains results of the best-fitting models from grid A.

Star	Verma et al. (2014)	Verma et al. (2019)	This work
16 Cyg A	0.231–0.251	0.232–0.263	0.220–0.242
16 Cyg B	0.218–0.266	0.245–0.265	0.209–0.233
KIC 6106415	–	0.210–0.236	0.194–0.224
KIC 6116048	–	0.216–0.238	0.192–0.224

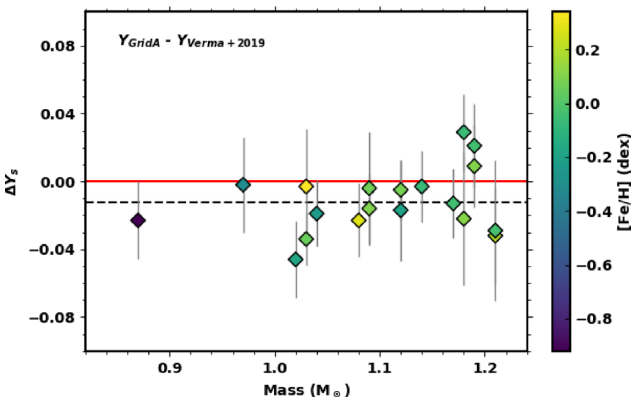

Figure 10. Difference between surface helium abundance values from grid A and those based on glitch analysis from Verma et al. (2019). The colour-coding is with respect to metallicity. The black dashed line and the solid red line represent the bias (~ 0.012) and the zero level, respectively.

sample. In our sample all values of the initial helium abundance are 1σ consistent with a value above the primordial helium abundance. Hence, we find no significant indication for the problem reported by other authors in our study.

This work gives a detailed insight and quantifies the biases and systematic uncertainties that arise from the treatment of the initial helium abundance in stellar grids. This is important for the ESA's PLATO preparatory work concerning the construction of stellar model grids to be used to infer stellar parameters for stars to be observed by the PLATO mission. The findings in this work are encouraging in a way that the systematic uncertainties on radius and mass found when adopting different approaches for the initial helium abundance determination lie within the required PLATO accuracy limits for stellar parameters of exoplanet-hosts. However, we call attention to the fact that the accuracy limits on the age may not be satisfied.

ACKNOWLEDGEMENTS

The authors acknowledge the dedicated team behind the NASA'S *Kepler* missions. BN thanks Verma Kuldeep, Achim Weiss, and the Stellar Evolution research group at Max-Planck-Institut für Astrophysik (MPA) for the useful comments on this article. BN also acknowledges postdoctoral funding from the Alexander von Humboldt Foundation. AGH, JCS, and BN acknowledge funding support from Spanish public funds (including FEDER funds) for research under projects ESP2017-87676-C5-2-R and ESP2017-87676-C5-5-R. TLC acknowledges support from the European Union's Horizon 2020 research and innovation programme under the Marie Skłodowska-Curie grant agreement no. 792848 (PULSATION). JF wishes to honor the memory of Johannes Andersen, recently passed way. JF acknowledges funding from POCH and Portuguese FCT grant SFRH/BSAB/143060/2018. CITEUC is funded by National Funds through FCT – Foundation for Science and Technology (projects UID-PB/00611/2020). MSC is supported by national funds through Fundação para a Ciência e a Tecnologia (FCT, Portugal) – in the form of a work contract and through the research grants UIDB/04434/2020, UIDP/04434/2020, and PTDC/FIS-AST/30389/2017, and by FEDER – Fundo Europeu de Desenvolvimento Regional through COMPETE2020 – Programa Operacional Competitividade e Internacionalizácao (grant: POCI-01-0145-FEDER-030389). AGH also acknowledges support from 'FEDER/Junta de Andalucía-Consejería de Economía y Conocimiento' under project E-FQM-041-UGR18 by Universidad de Granada. JCS also acknowledges support from project RYC-2012-09913 under the 'Ramón y Cajal' program of the Spanish Ministry of Science and Education. JC is funded by the Fundamental Research Funds for the Central Universities (grant: 19lgpy278). BA acknowledges support from the FCT PhD programme PD/BD/135226/2017. We thank the reviewer for the constructive remarks.

DATA AVAILABILITY

The data underlying this article are available in the article. The details of the 'inlist' files used in the stellar evolution code (MESA) are described in Section 2.2 and can easily be reproduced.

REFERENCES

Adibekyan V. Z., Sousa S. G., Santos N. C., Delgado Mena E., González Hernández J. I., Israelian G., Mayor M., Khachatryan G., 2012, A&A, 545, A32

Aerts C., Christensen-Dalsgaard J., Kurtz D. W., 2010, Asteroseismology. Springer, Netherlands

Downloaded from https://academic.oup.com/mnras/article/500/1/54/5925370 by Inst. Astrofisica Andalucia CSIC user on 10 February 2021

Allen C. W., 1976, Astrophysical Quantities, 3rd edn. Atholone Press, London
Anders E., Grevesse N., 1989, Geochim. Cosmochim. Acta, 53, 197
Angelou G. C., Bellinger E. P., Hekker S., Mints A., Elsworth Y., Basu S., Weiss A., 2020, MNRAS, 493, 4987
Asplund M., Grevesse N., Sauval A. J., Scott P., 2009, ARA&A, 47, 481
Badnell N. R., Bautista M. A., Butler K., Delahaye F., Mendoza C., Palmeri P., Zeippen C. J., Seaton M. J., 2005, MNRAS, 360, 458
Bahcall J. N., Serenelli A. M., Pinsonneault M., 2004, ApJ, 614, 464
Ball W. H., Gizon L., 2014, A&A, 568, A123
Ball W. H., Gizon L., 2017, A&A, 600, A128
Balser D. S., 2006, AJ, 132, 2326
Basu S., Antia H. M., 2004, in Danesy D., ed., ESA SP-559: SOHO 14 Helio- and Asteroseismology: Towards a Golden Future. ESA Publication Division, Noordwijk, p. 317
Basu S., Kinnane A., 2018, ApJ, 869, 8
Basu S., Chaplin W. J., Elsworth Y., 2010, ApJ, 710, 1596
Belkacem K., Samadi R., Mosser B., Goupil M. J., Ludwig H. G., 2013, in Shibahashi H., Lynas-Gray A. E., eds, ASP Conf. Ser., Vol. 479, Progress in Physics of the Sun and Stars: A New Era in Helio- and Asteroseismology. Astronomical Society of the Pacific, Hakone - Japan, p. 61
Bellinger E. P., Hekker S., Angelou G. C., Stokholm A., Basu S., 2019, A&A, 622, A130
Boltzmann L., 1884, Ann. Phys., 258, 291
Bonaca A. et al., 2012, ApJ, 755, L12
Broomhall A. M. et al., 2014, MNRAS, 440, 1828
Brown T. M., Gilliland R. L., Noyes R. W., Ramsey L. W., 1991, ApJ, 368, 599
Buchhave L. A., Latham D. W., 2015, ApJ, 808, 187
Casagrande L., Flynn C., Portinari L., Girardi L., Jimenez R., 2007, MNRAS, 382, 1516
Casagrande L. et al., 2014, ApJ, 787, 110
Christensen-Dalsgaard J., Thompson M. J., 1997, MNRAS, 284, 527
Connelly J. N., Bizzarro M., Krot A. N., Nordlund Å., Wielandt D., Ivanova M. A., 2012, Science, 338, 651
Corsaro E., De Ridder J., García R. A., 2015, A&A, 578, A76
Cyburt R. H., Fields B. D., Olive K. A., 2003, Phys. Lett. B, 567, 227
Deal M., Escobar M. E., Vauclair S., Vauclair G., Hui-Bon-Hoa A., Richard O., 2017, A&A, 601, A127
Deal M., Alecian G., Lebreton Y., Goupil M. J., Marques J. P., LeBlanc F., Morel P., Pichon B., 2018, A&a, 618, A10
Demarque P., Guenther D. B., Li L. H., Mazumdar A., Straka C. W., 2008, Ap&SS, 316, 31
Dréau G., Cunha M. S., Vrard M., Avelino P. P., 2020, MNRAS, 497, 1008
Dziembowski W. A., Paterno L., Ventura R., 1988, A&A, 200, 213
Emilio M., Kuhn J. R., Bush R. I., Scholl I. F., 2012, ApJ, 750, 135
Ferguson J. W., Alexander D. R., Allard F., Barman T., Bodnarik J. G., Hauschildt P. H., Heffner-Wong A., Tamanai A., 2005, ApJ, 623, 585
Frandsen S. et al., 2018, A&A, 613, A53
Gai N., Basu S., Chaplin W. J., Elsworth Y., 2011, ApJ, 730, 63
Gough D. O., 1990, Proceedings of the Oji International Seminar, Comments on Helioseismic Inference. Osaki, Yoji and Shibahashi, Hiromoto, Hakone - Japan, p. 283
Gough D. O., Thompson M. J., 1988, in Christensen-Dalsgaard J., Frandsen S., eds, IAU Symp., Vol. 123, Advances in Helio- and Asteroseismology. Symposium of the International Astronomical Union, Aarhus - Denmark, p. 155
Grevesse N., Sauval A. J., 1998, Space Sci. Rev., 85, 161
Grevesse N., Asplund M., Sauval A. J., 2007, Space Sci. Rev., 130, 105
Higl J., Weiss A., 2017, A&A, 608, A62
Houdek G., Gough D. O., 2007, MNRAS, 375, 861
Iglesias C. A., Rogers F. J., 1996, ApJ, 464, 943
Imbriani G. et al., 2005, EPJ A, 25, 455
Jiang C. et al., 2020, ApJ, 896, 65
Jimenez R., Flynn C., MacDonald J., Gibson B. K., 2003, Science, 299, 1552
Jørgensen A. C. S. et al., 2020, MNRAS, 495, 4965
Kippenhahn R., Weigert A., Weiss A., 2012, Stellar Structure and Evolution. Springer, Berlin, Heidelberg
Kjeldsen H., Bedding T. R., 1995, A&A, 293, 87
Kjeldsen H., Bedding T. R., Christensen-Dalsgaard J., 2008, ApJ, 683, L175
Kunz R., Fey M., Jaeger M., Mayer A., Hammer J. W., Staudt G., Harissopulos S., Paradellis T., 2002, ApJ, 567, 643
Lebreton Y., Goupil M. J., 2014, A&A, 569, A21
Li T., Bedding T. R., Christensen-Dalsgaard J., Stello D., Li Y., Keen M. A., 2020, MNRAS, 495, 3431
Lodders K., 2003, ApJ, 591, 1220
Lund M. N. et al., 2017, ApJ, 835, 172
Malagnini M. L., Morossi C., 1997, A&A, 326, 736
Mathur S. et al., 2012, ApJ, 749, 152
Mazumdar A. et al., 2014, ApJ, 782, 18
Metcalfe T. S. et al., 2010, ApJ, 723, 1583
Metcalfe T. S. et al., 2014, ApJS, 214, 27
Miglio A. et al., 2010, A&A, 520, L6
Moedas N., Nsamba B., Clara M. T., 2020, preprint (arXiv:2007.03362)
Montambaux G., 2018, Foundations of Physics, 48, 395
Monteiro M. J. P. F. G., Thompson M. J., 2005, MNRAS, 361, 1187
Mosser B. et al., 2013, A&A, 550, A126
Nsamba B., Monteiro M. J. P. F. G., Campante T. L., Reese D. R., White T. R., García Hernández A., Jiang C., 2017, EPJ Web Conf, 160, 05010
Nsamba B., Campante T. L., Monteiro M. J. P. F. G., Cunha M. S., Rendle B. M., Reese D. R., Verma K., 2018a, MNRAS, 477, 5052
Nsamba B., Monteiro M. J. P. F. G., Campante T. L., Cunha M. S., Sousa S. G., 2018b, MNRAS, 479, L55
Nsamba B., Campante T. L., Monteiro M. J. P. F. G., Cunha M. S., Sousa S. G., 2019, Front. Astron. Space Sci., 6, 25
Paul H., Greenberger D. M., Stenholm S. T., Schleich W. P., 2015, Phys. Scr. Vol.T, 165, 014027
Paxton B. et al., 2013, ApJS, 208, 4
Paxton B. et al., 2015, ApJS, 220, 15
Paxton B. et al., 2018, ApJS, 234, 34
Pinsonneault M. H., An D., Molenda-Żakowicz J., Chaplin W. J., Metcalfe T. S., Bruntt H., 2012, ApJS, 199, 30
Pinsonneault M. H. et al., 2014, ApJS, 215, 19
Prša A. et al., 2016, AJ, 152, 41
Ramírez I., Meléndez J., Asplund M., 2009, A&A, 508, L17
Rauer H. et al., 2014, Exper. Astron., 38, 249
Rendle B. M. et al., 2019, MNRAS, 484, 771
Rodrigues T. S. et al., 2017, MNRAS, 467, 1433
Rogers F. J., Nayfonov A., 2002, ApJ, 576, 1064
Roxburgh I. W., Vorontsov S. V., 2003, A&A, 411, 215
Seaton M. J., 2005, MNRAS, 362, L1
Serenelli A. M., Basu S., 2010, ApJ, 719, 865
Serenelli A. et al., 2020, preprint (arXiv:2006.10868)
Silva Aguirre V. et al., 2015, MNRAS, 452, 2127
Silva Aguirre V. et al., 2017, ApJ, 835, 173
Sonoi T., Samadi R., Belkacem K., Ludwig H. G., Caffau E., Mosser B., 2015, A&A, 583, A112
Suárez J. C., García Hernández A., Moya A., Rodrigo C., Solano E., Garrido R., Rodón J. R., 2014, A&A, 563, A7
Théado S., Vauclair S., Castro M., Charpinet S., Dolez N., 2005, A&A, 437, 553
Thoul A. A., Bahcall J. N., Loeb A., 1994, ApJ, 421, 828
Townsend R. H. D., Teitler S. A., 2013, MNRAS, 435, 3406
Turcotte S., Richer J., Michaud G., Iglesias C. A., Rogers F. J., 1998, ApJ, 504, 539
Ulrich R. K., 1986, ApJ, 306, L37
Valle G., Dell'Omodarme M., Prada Moroni P. G., Degl'Innocenti S., 2014, A&A, 561, A125
Valle G., Dell'Omodarme M., Prada Moroni P. G., Degl'Innocenti S., 2015, A&A, 575, A12
Valle G., Dell'Omodarme M., Prada Moroni P. G., Degl'Innocenti S., 2020, A&A, 635, A77
Verma K. et al., 2014, ApJ, 790, 138
Verma K., Raodeo K., Antia H. M., Mazumdar A., Basu S., Lund M. N., Silva Aguirre V., 2017, ApJ, 837, 47

Downloaded from https://academic.oup.com/mnras/article/500/1/54/5925370 by Inst. Astrofisica Andalucia CSIC user on 10 February 2021

Verma K., Raodeo K., Basu S., Silva Aguirre V., Mazumdar A., Mosumgaard J. R., Lund M. N., Ranadive P., 2019, MNRAS, 483, 4678
Vincenzo F., Miglio A., Kobayashi C., Mackereth J. T., Montalban J., 2019, A&A, 630, A125
Vrard M. et al., 2015, A&A, 579, A84
Weiss A., Schlattl H., 2008, Ap&SS, 316, 99
White T. R. et al., 2017, A&A, 601, A82
Joyce M., Chaboyer B., 2018a, ApJ, 864, 99
Joyce M., Chaboyer B., 2018b, ApJ, 856, 10

SUPPORTING INFORMATION

Supplementary data are available at *MNRAS* online.

Table A1. Stellar Properties for our sample derived from grids A, B, and C.

Please note: Oxford University Press is not responsible for the content or functionality of any supporting materials supplied by the authors. Any queries (other than missing material) should be directed to the corresponding author for the article.

APPENDIX

The inferred stellar properties from the grids A, B, and C are published in the online version of this paper. A description of all fields available is given in Table A1. A similar table is also available in machine-readable form.

Table A1. Stellar properties for our sample derived from grids A, B, and C.

Item	Description
KIC	Kepler Input Catalog Identifier
Mass	Mass in solar units
$\sigma_{\rm Mass}$	Mass uncertainty in solar units
Rad	Radius in solar units
$\sigma_{\rm Rad}$	Radius uncertainty in solar units
log g	Surface gravity in dex
$\sigma_{\rm logg}$	Surface gravity uncertainty in dex
Age	Age in units of Myr
$\sigma_{\rm Age}$	Age uncertainty in units of Myr
Lum	Luminosity in solar units
$\sigma_{\rm Lum}$	Luminosity uncertainty in solar units
Rho	Density in g cm^{-3}
$\sigma_{\rm Rho}$	Density uncertainty in g cm^{-3}
Xi	Fractional initial hydrogen abundance
$\sigma_{\rm Xi}$	Fractional initial hydrogen abundance uncertainty
Yi	Fractional initial helium abundance
$\sigma_{\rm Yi}$	Fractional initial helium abundance uncertainty
Xs	Fractional surface hydrogen abundance
$\sigma_{\rm Xs}$	Fractional surface hydrogen abundance uncertainty
Ys	Fractional surface helium abundance
$\sigma_{\rm Ys}$	Fractional surface helium abundance uncertainty
$\alpha_{\rm mlt}$	Mixing length parameter
$\sigma_{\alpha_{\rm mlt}}$	Mixing length parameter uncertainty

This paper has been typeset from a TEX/LATEX file prepared by the author.

Downloaded from https://academic.oup.com/mnras/article/500/1/54/5925370 by Inst. Astrofisica Andalucia CSIC user on 10 February 2021